Chapter 14

Global Circulations

14.1 Simple model of global radiation balance

The earth receives energy from the sun in the form of visible, near-infrared, and ultraviolet radiation. Most of this energy is either reflected back to space by clouds and other bright surfaces (about 30%), or is absorbed by the earth's surface. A significant fraction of the near-infrared component is absorbed by water vapor. However, since the greatest amount of vapor is found at low levels near the surface, that is where the near-infrared is preferentially absorbed in the atmosphere. Ultraviolet radiation, which forms only a small fraction of the energy coming from the sun, is mostly absorbed by ozone in the stratosphere.

Figure 14.1 illustrates a simple model of the gross radiation balance of the earth. The solar flux at the earth's orbit is $F_s = 1370$ W m^{-2}. If a fraction $A = 0.3$ is reflected by the earth, then the amount of solar radiation absorbed by the earth is equal to $F_s(1 - A)$ times the projected area of the earth πR^2, where $R = 6370$ km is the earth's radius. This amounts to 122 PW. (One petawatt = 1 PW = 10^{15} W.)

This input of energy is balanced by the outflow of thermal radiation. The radiative temperature of the earth T_{rad} is the temperature which would result in this outflow if the earth radiated like a black body:

$$\pi R^2 F_s(1 - A) = 4\pi R^2 \sigma T_{rad}^4 \tag{14.1}$$

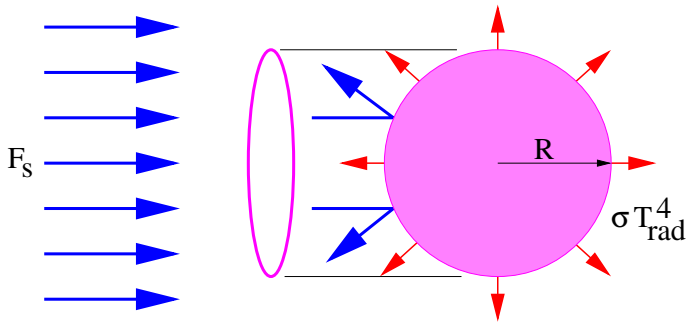

Figure 14.1: Gross radiation balance of the earth. Incoming solar radiation with flux F_s must be balanced by losses from reflection and infrared black body emission.

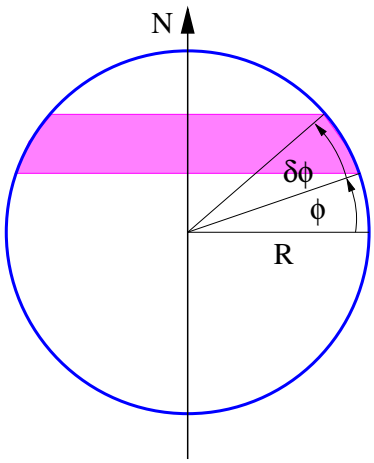

Figure 14.2: Sketch of geometry used in the calculation of the latitudinal dependence of radiative temperature at the equinox.

where $\sigma = 5.67 \times 10^{-8}$ W m^{-2} K^{-4}. Solving for T_{rad} results in

$$T_{rad} = \left[\frac{F_s(1-A)}{4\sigma}\right]^{1/4}, \tag{14.2}$$

which for the given numbers yields $T_{rad} = 255$ K.

The radiative temperature thus calculated is significantly colder than the mean temperature of the earth's surface, which is near 288 K. This is because the earth's atmosphere is somewhat opaque to the thermal infrared radiation emitted by the surface of the earth, which means that the actual radiation to space occurs not from the surface, but from some higher level in the atmosphere, which is colder. The opacity of the atmosphere to thermal infrared radiation has little to do with the main atmospheric constituents, nitrogen and oxygen, but is caused primarily by the trace gases carbon dioxide, water vapor, methane, and especially in the stratosphere, ozone. In the troposphere, water vapor is the most important of these gases. The elevation of the surface temperature above the radiative temperature is called the *greenhouse effect*.

14.2 Latitudinal energy transfer

Energy deposition is not uniform with latitude. Less solar radiation is deposited at high latitudes than low, and in the winter than in the summer hemisphere. A *local* equilibrium temperature can be computed at each latitude, but the resulting temperature distribution has a much steeper decline toward the poles than is observed. Thus, energy must be transported from the tropical regions toward the poles.

Let us make a quantitative calculation of this effect for the case in which the sun is directly over the equator, i. e., at the equinox. The key issue is the actual versus the projected area of a latitudinal strip of the earth's surface, as illustrated in figure 14.2. The actual area of the strip of earth's surface illustrated in this figure is $\delta S = 2\pi R \cos\phi \cdot R\delta\phi$, while the projected

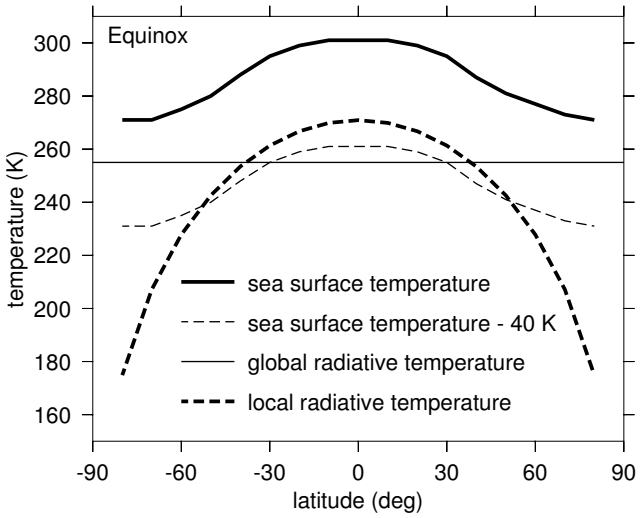

Figure 14.3: Annual and longitudinal mean of sea surface temperature, sea surface temperature -40 K, global mean radiative temperature and latitudinal distribution of radiative temperature at the equinox.

area of this strip as seen from the sun is $\delta S_p = 2R\cos\phi \cdot R\cos\phi\delta\phi$. Assuming albedo A at latitude ϕ, the energy balance at this latitude is $F_s(1-A)\delta S_p = \sigma T_{rad}^4 \delta S$, resulting in a radiative temperature there of

$$T_{rad}(\phi) = \left[\frac{F_s(1-A)\cos\phi}{\pi\sigma}\right]^{1/4}. \tag{14.3}$$

Figure 14.3 shows the latitudinal distribution of radiative temperature as well as the global radiative temperature and the mean sea surface temperature as a function of latitude. Also plotted is the sea surface temperature minus 40 K, slightly greater than the difference between the surface temperature and the radiative temperature in the globally uniform case. This can be taken as an approximation of the actual local radiative temperature. Within 50° of the equator the predicted radiative temperature exceeds the actual value, whereas at higher latitudes the reverse is true. This implies lateral export of energy by the oceans and atmosphere from low latitudes to high, i. e., transport of energy down the temperature gradient. In other words, there is a net flow of energy into the atmosphere and oceans at low latitudes, followed by transport to high latitudes, where there is net export.

Figure 14.4 shows that this transport actually does take place. On an annual average, import of energy by radiation at the top of the atmosphere exceeds export by $2 + 5 + 2.5 = 9.5$ PW between 30°S and 30°N. the same amount is exported to space at higher latitudes. The poleward transport of energy is shared almost equally by the atmosphere and the ocean, with the ocean contributing slightly more.

Within 10° of the equator, the atmospheric absorption of solar radiation and the emission of infrared are nearly in balance, so that the net absorption is only about 2 PW. The absorbed energy is exported to higher latitudes. This compares with a solar input of $F_s(1-A)\cdot 2R^2\cos^2\phi\delta\phi$, which equals 27 PW for $\phi = 0$ and $\delta\phi = 20/57.3$radians. Thus, the atmosphere in this band exports laterally only about 7% of the incoming solar radiation.

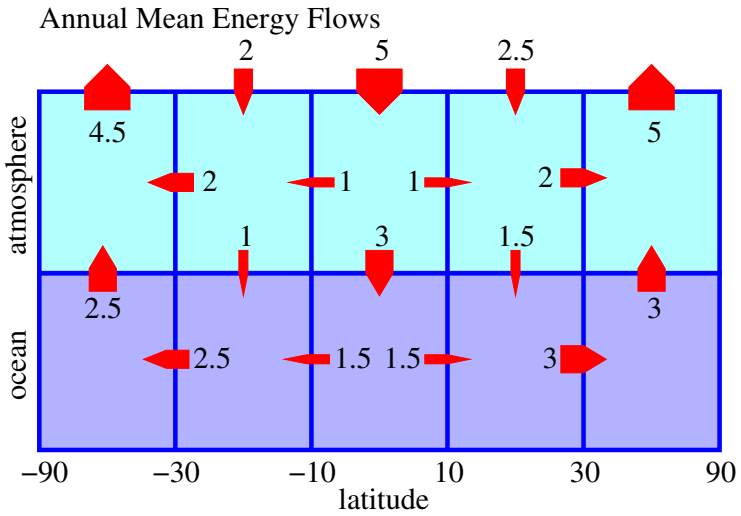

Figure 14.4: Annually averaged net energy flows in petawatts (10^{15} W; fluid transport plus radiation) between space and various latitudinal segments of the atmosphere and ocean. Data adapted from Peixoto and Oort (1992).

However, an additional 11%, or 3 PW of incoming solar energy travels indirectly to higher latitudes via the oceans.

The transition between net inflow from space to net outflow to space occurs near latitudes ±30°. This is lower in latitude than suggested by the estimate in figure 14.3 where this transition occurs nearer 50°. However, we must remember that figure 14.3 is based on rather loose arguments.

Figure 14.5 shows the global energy flows as in figure 14.4, except averaged over December, January, and February only, i. e., during the northern winter. As would be expected from the southerly position of the sun during this period, there is a net inflow of energy into the southern hemisphere and a net outflow in the northern hemisphere. These hemispheric imbalances are partially compensated by flow of energy from south to north in both the atmosphere and the ocean. However, this flow doesn't account for all of the southern hemisphere gains and northern hemisphere losses. Substantial warming with time occurs in the southern hemisphere as well as substantial cooling north of the equator. This heat storage effect is most important in the oceans, as the oceanic heat capacity is much higher than that of the atmosphere. The situation for the northern summer is nearly a mirror image of that for the northern winter.

14.3 Vertical energy transfer

14.3.1 Atmosphere

As noted above, solar energy is deposited at the surface and at low levels in the atmosphere, while departing thermal infrared radiation is emitted on the average at atmospheric temperatures of 255 K, which corresponds to an average elevation of about 6 km. Two processes transport this energy upward, thermal radiation and convection. It turns out that radiative

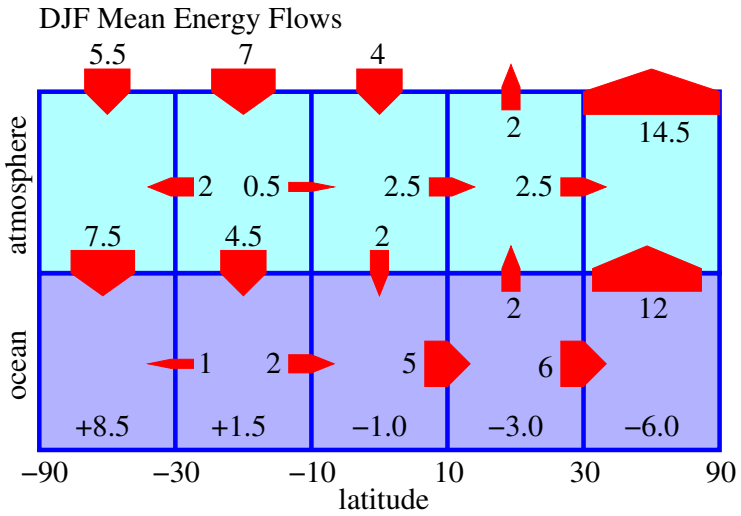

Figure 14.5: December-January-February averaged net energy flows (in petawatts; fluid transport plus radiation) between space and various latitudinal segments of the atmosphere and ocean. The numbers at the bottom are the rates at which energy is stored in the ocean segments. Zero storage is assumed for the atmosphere. Data adapted from Peixoto and Oort (1992).

transfer is incapable by itself of performing the necessary transport, because the resulting vertical temperature profile is unstable to convection below a certain level. The layer in which convection occurs in the atmosphere is called the *troposphere*. The convectively stable layer above the troposphere is called the *stratosphere*, and the boundary between the two layers is called the *tropopause*.

In the stratospheric layer the atmosphere is close to *radiative equilibrium*, i. e., the vertical radiative energy fluxes are such that zero net heating occurs at each level in this layer. We showed in the previous section that the tropical atmosphere within 10° of the equator has small lateral fluxes compared to the upward and downward energy fluxes due to solar radiation, thermal radiation, and convection. Thus, the predominant balance in the tropical troposphere is nearly one of *radiative-convective equilibrium*, i. e., one in which convective heating at each level is balanced by radiative cooling.

Since the surface of the earth is nearly covered by water, the earth's atmosphere contains a great deal of water vapor. Since rising convective parcels cool in their ascent, they eventually reach a level, called the lifting condensation level (LCL), at which the water vapor in the parcel begins to condense. This has three consequences. First, the condensation releases latent heat, resulting in higher temperatures in ascent than in a parcel without condensation. Second, much of this condensed water falls out of the parcel as precipitation. As a result, the parcel follows a different thermodynamic trajectory in the descending part of its convective cycle. Third, the small water drops and ice crystals which form when a parcel reaches the LCL and the freezing level interact strongly with solar and thermal radiation, thus modifying the radiative transfer of energy in the atmosphere. The net result is a complex and interesting system with many stubborn scientific uncertainties of importance to weather and climate.

14.3.2 Ocean

Water is highly opaque to infrared radiative transfer, and even in the clearest ocean water most of the solar radiation is deposited in the upper 100 m or so. Convection occurs in the ocean in regions where the high density of cold, salty surface water is sufficient to produce negative parcel buoyancies. This sinking water becomes the source of deep ocean water. The upward return circulation occurs at low latitudes far from the sinking motion, which occurs only in preferred regions at high latitudes. The complete circulation system is called the thermohaline circulation. Our knowledge of the details of this circulation is quite sketchy at this point. In particular, the mechanisms governing the upwelling of deep water are not well understood.

Just as the budget of moisture is inextricably intertwined with the budget of energy in the atmosphere, the budget of salt plays a crucial role in the energy budget in the ocean. This is because salt content has a large effect on ocean water density. Salt content is increased as a result of evaporation at the ocean surface, and is decreased by the inflow of fresh water into the ocean from rivers and precipitation.

The salt content of the ocean is measured in terms of *salinity* S. Salinity is defined officially in terms of the electrical conductivity of ocean water. However, in practical terms the salinity is just the mass of dissolved salts per unit mass of water, measured in grams of salt per kilogram of fresh water.

14.4 Observational examples

In this section we diagose various observational data sets to illustrate the principles of geophysical fluid dynamics. The National Centers for Environmental Prediction operate the US's national global atmospheric forecast model, called the Global Forecast System or GFS. We use 12 hour predictions from this model to characterize the atmosphere. The 12 hour forecast is used because it close enough to the initialization that the forecast is unlikely to be far from the truth, but is far enough that various predicted quantities like precipitation have equilibrated.

14.4.1 Zonal atmospheric means

We begin by looking at zonal atmospheric means for a six day time interval in the northern summer, 26 July through 4 August 2010, as an example. Figure 14.6 shows the mean zonal wind and potential temperature structure of the troposphere for the above period. Note that the strongest winds are the westerly jet stream winds near the tropopause in the southern hemisphere. The northern hemisphere jet stream is significantly weaker. With minor exception, westerly winds exist at all elevations in the middle latitudes. Easterly winds dominate in the tropics and the winter (south) polar region, though the interface between easterlies and westerlies in the winter hemisphere is tilted to the north, so that between roughly 20° S and 30° S, low-level easterlies (tradewinds) are topped by upper level westerlies.

The red lines in figure 14.6are contours of potential temperature. They are nearly horizontal in the tropics, but tilt sharply upwards toward the poles in the middle latitude. This

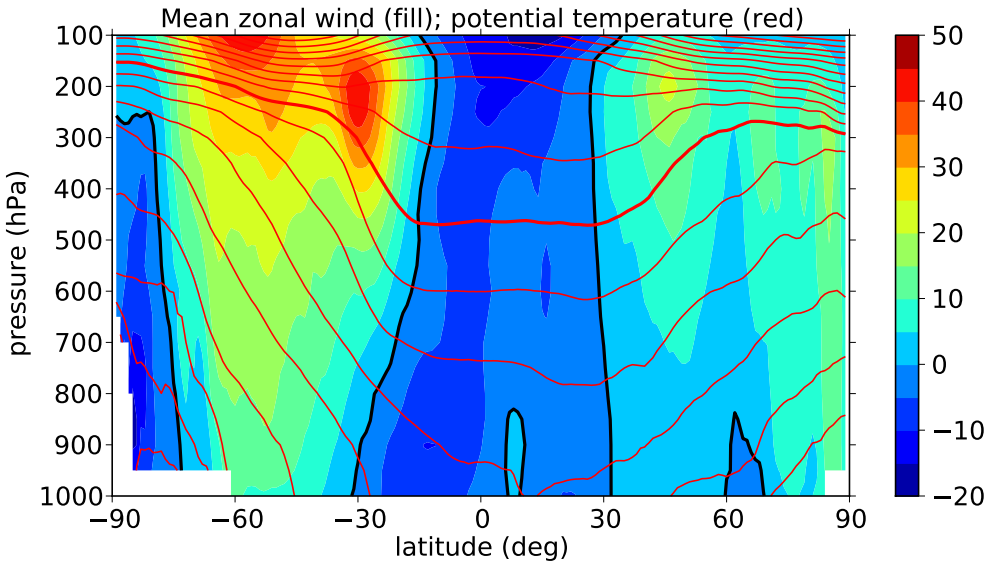

Figure 14.6: Zonal mean zonal wind (filled contours; m s^{-1}) and potential temperature (red contours, 10 K contour interval, heavy contour 330 K). Northern summer.

tilt represents a horizontal temperature gradient, which is coupled via the thermal wind equation with the strong vertical shear underneath the jet streams. This gradient is much stronger in the southern hemisphere. The vertical gradient of potential temperature at upper levels, reflected in the decreased spacing of potential temperature contours there, indicates the lower stratosphere.

Figure 14.7 shows the zonal mean meridional wind. The dominant features are the low-level southerlies and the high level northerlies near the equator. These are part of the Hadley circulation, which is discussed below. Less intense but still noteworthy are the low-level northerlies in the range $40° - 70°$ S and the corresponding southerlies at upper levels. These form part of the Ferrel circulation. A weak northern hemisphere counterpart exists as well. Comparison with figure 14.6 shows that poleward winds in each hemisphere are accompanied by westerlies, a result explicable in terms of the effect of the Coriolis force.

Figure 14.8 shows the zonal mean potential temperature contours and color contours of the Ertel potential vorticity. In this plot stratospheric values of the potential vorticity dominate values in the troposphere because they are so much larger in magnitude. Figure 14.9 shows a similar plot, but with the contour range weighted toward tropospheric values. Note that the horizontal gradient of potential vorticity is weak in the tropics and middle latitudes, becoming much stronger poleward of $\approx 60°$. This increase is related to the cyclonic vorticity which exists on the poleward side of the jet streams. The effect is stronger in the winter hemisphere.

Figure 14.10 shows the zonal mean meridional circulation in the troposphere as represented by a streamfunction. This is obtained as follows. In pressure coordinates the zonally

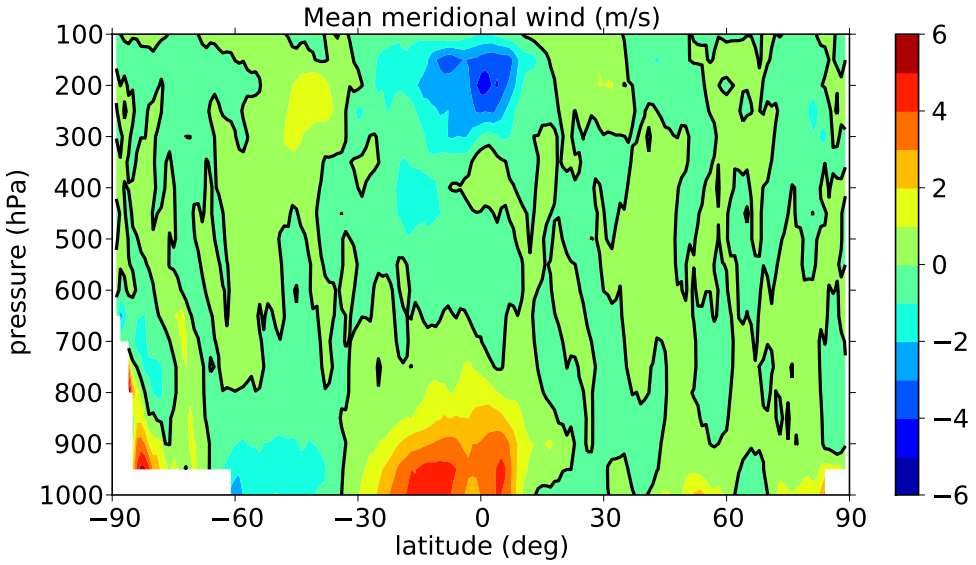

Figure 14.7: Zonal mean meridional wind (color contours). The heavy black contours indicate zero meridional wind.

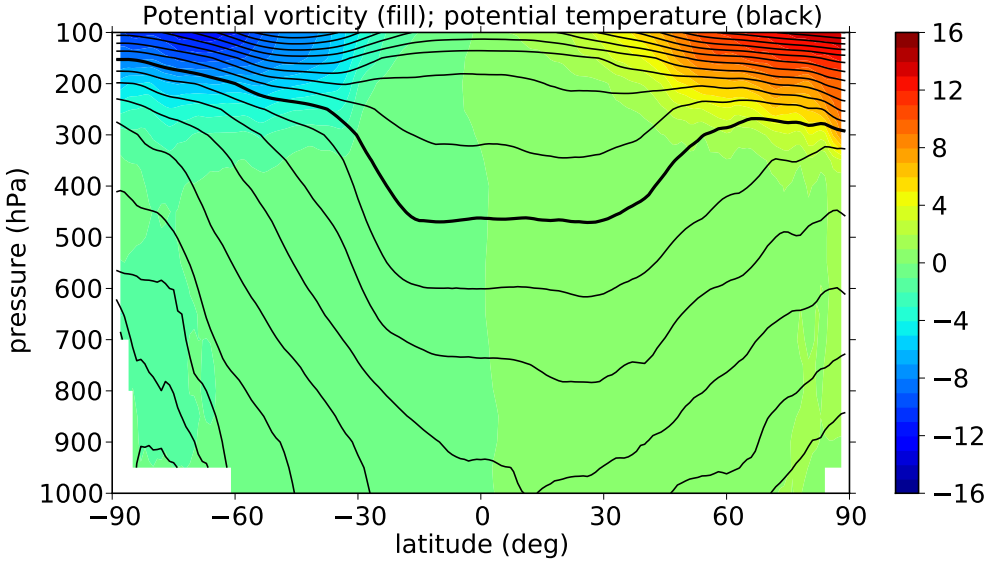

Figure 14.8: Zonal mean potential vorticity (filled contours, PV units) and potential temperature (black contours). Northern summer.

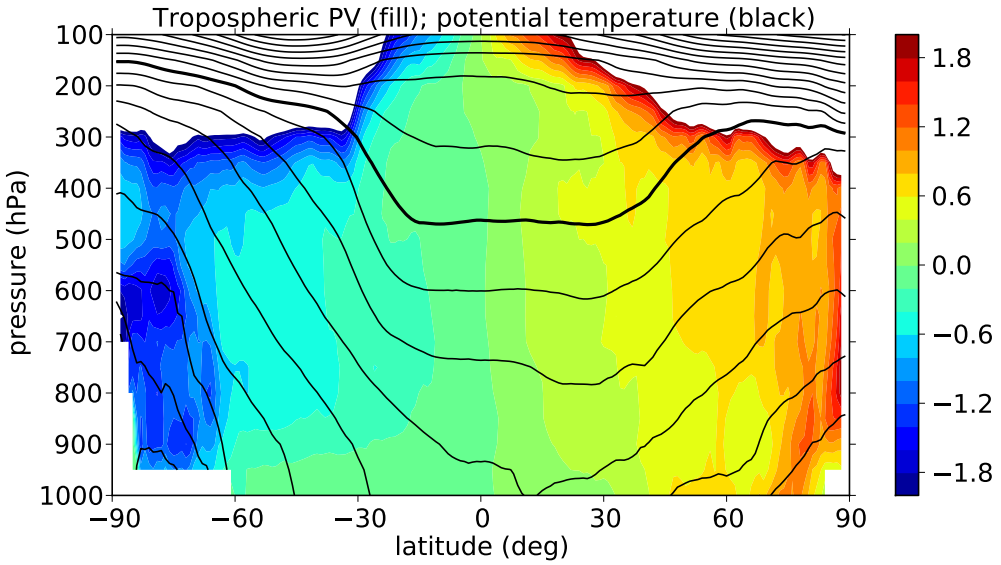

Figure 14.9: Potential vorticity and potential temperature as in figure 14.8 except that potential vorticity contours are weighted toward tropospheric values. Northern summer.

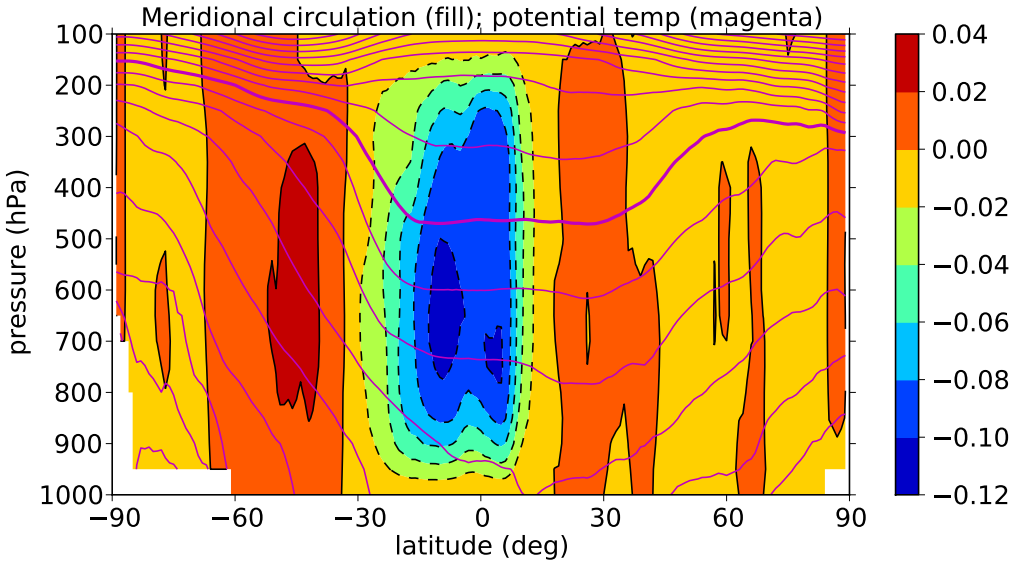

Figure 14.10: Zonal mean streamfunction ψ (color contours) and potential temperature (magenta contours) in the latitude-pressure plane. Northern summer.

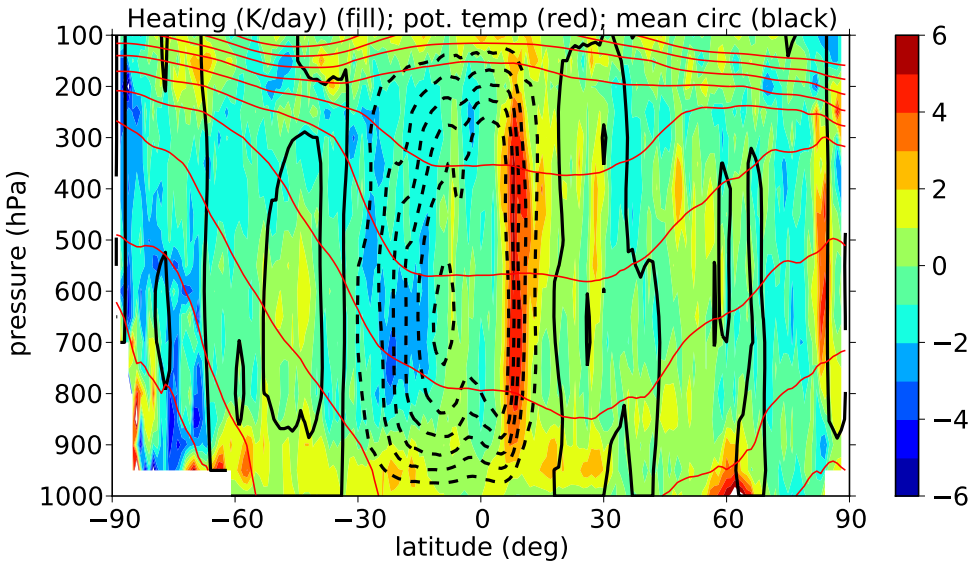

Figure 14.11: Zonal mean heating rate (filled contours, K d^{-1}), potential temperature (red contours), and streamfunction (black contours). Northern summer.

symmetric mass continuity equation for the atmosphere is

$$\frac{1}{a}\frac{\partial v \cos\phi}{\partial \phi} + \frac{\partial \omega}{\partial p} = 0 \tag{14.4}$$

where v is the meridional wind, ω is the pressure vertical velocity, ϕ is the latitude, p is the pressure, and a is the radius of the earth. Given this relationship, we can define a streamfunction ψ such that

$$v = \frac{a}{\cos\phi}\frac{\partial \psi}{\partial p} \qquad \omega = -\frac{\partial \psi}{\partial \phi}. \tag{14.5}$$

Velocity vectors are everywhere tangent to streamfunction contours and the flux of mass is inversely proportional to their spacing. The flow is counter-clockwise in figure 14.5 around negative peaks in the streamfunction and clockwise around positive peaks. Thus, for instance, the closely packed vertical contours near 10^{circ} N represent rising air, while contours between 20° S and 40° S indicate air that is sinking. Over the equator the flow is southerly (to the north) at low levels and northerly at high levels.

The closed circulation over and to the south of the equator indicated by negative values of ψ in figure 14.5 is called the *Hadley circulation*. The upward branch of this circulation near 10° N consists of deep convection, which is represented in figure 14.11 by strong heating. The descent region between 15° S and 30° S is clear with strong radiative cooling.

Figure 14.12 suggests why convection associated with the Hadley circulation is located near 10° N; this is the latitude of the northern summer sea surface temperature (SST)

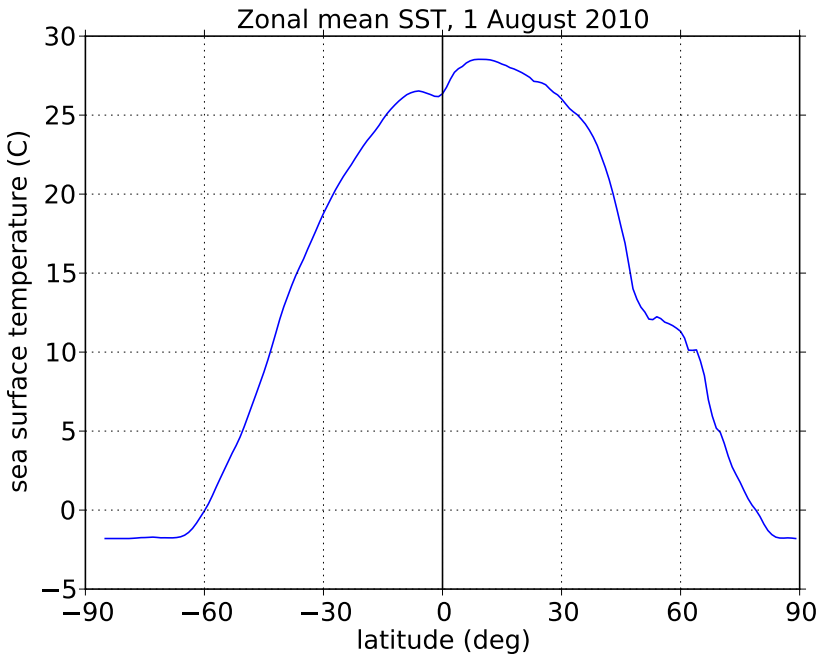

Figure 14.12: Zonal mean of Reynolds (Reynolds and Marsico 1993) sea surface temperature (with the continents masked out) for 1 August 2010.

maximum, and thus the location of the strongest energy transfer from the ocean to the atmosphere. The subsidence from the Hadley circulation convection is concentrated on the opposite side of the equator from the convection rather than to the north of the convection. This is qualitatively explained by the fact that compensating subsidence in a rotating environment is confined to within of order a Rossby radius of the region of ascent. The higher the latitude, the smaller the Rossby radius, so the upper level outflow descends broadly over the equatorial region to the south where the Rossby radius is very large.

Idealized models of the Hadley circulation treat this circulation as a steady, axisymmetric flow. This implies conservation of angular momentum as air rises in the convection and moves meridionally through the subsidence region, at least until it reaches the boundary layer, where frictional forces come into play. Such a model implies that the region of the circulation above the boundary layer should have uniform angular momentum (defined here as $m = u\cos\phi - \Omega a \sin^2\phi$ where u is the zonal wind, ϕ is the latitude, Ω is the rotation rate of the earth, and a is the earth's radius). Figure 14.13 shows that this is not true; streamlines cross contours of constant angular momentum, implying that time-dependent, nonaxisymmetric flow occurs even in the tropical belt.

Figure 14.6 illustrates this point more quantitatively. The actual mean zonal wind averaged over $100 - 300$ hPa is much less than the angular-momentum-conserving wind which starts from zero at the equator. This proves that nonaxisymmetric disturbances dominate to within $10^\circ - 15^\circ$ of the equator.

The examples presented here are derived from a short period in the northern summer. The southern summer shows flows that are basically reversed in latitude, as one might

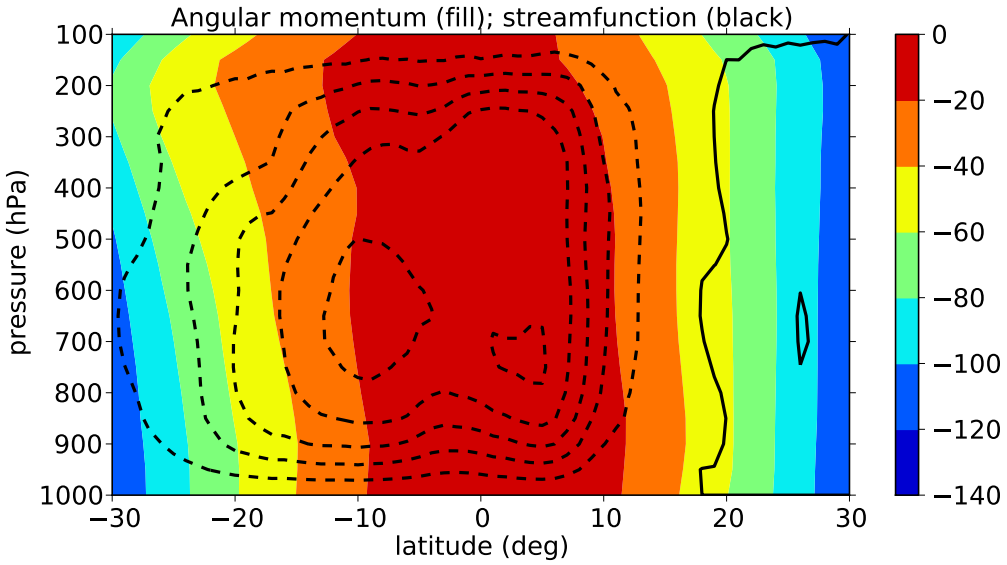

Figure 14.13: Zonal mean angular momentum (color contours, m s^{-1}) and meridional circulation for the tropical belt. Northern summer.

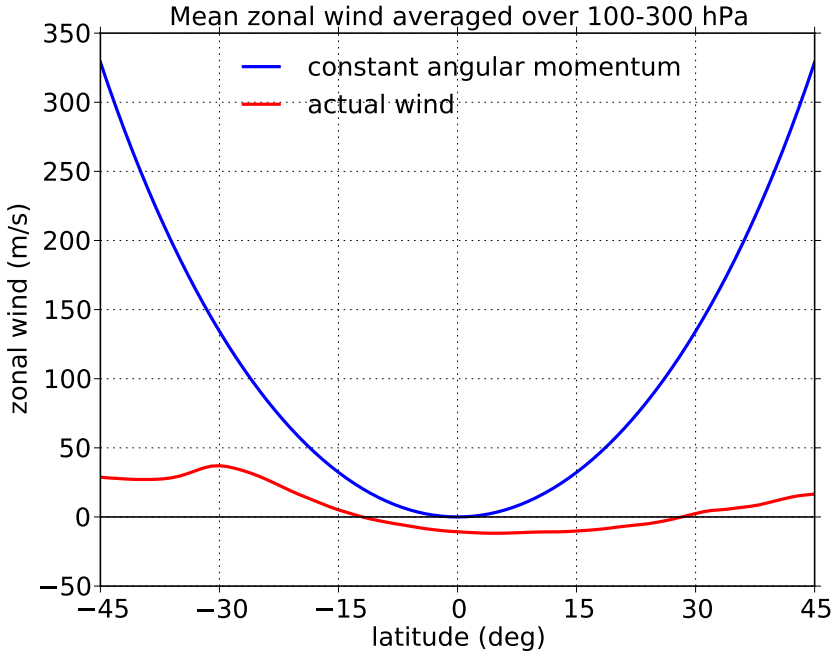

Figure 14.14: Mean zonal wind averaged over $100 - 300$ hPa (red line) and the angular-momentum-conserving wind resulting from a meridional displacement from the equator where the wind is zero (blue line). Any values above the blue line would indicate super-rotation.

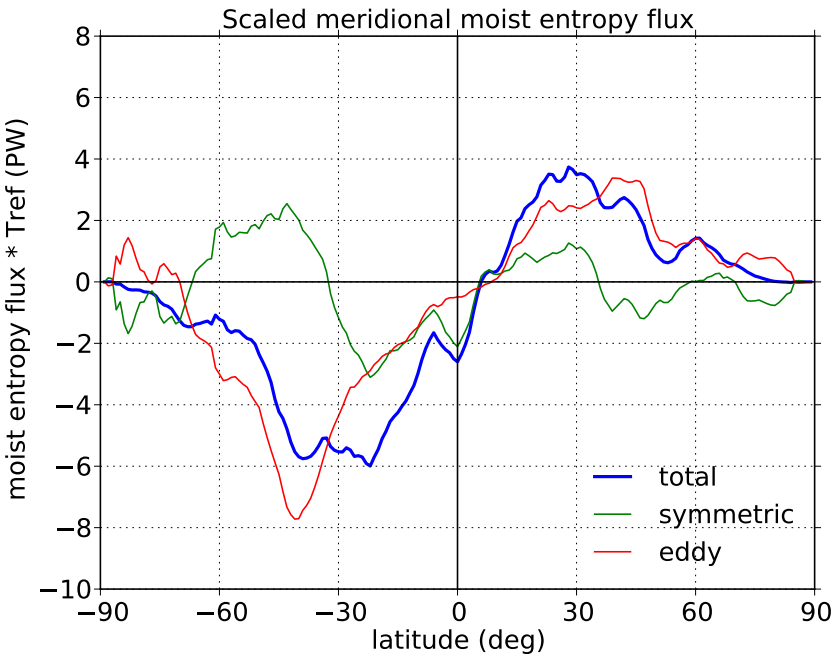

Figure 14.15: Scaled mean meridional moist entropy flux in the atmosphere. The scaling factor $T_{ref} = 300$ K converts the flux to power units, petawatts in this case. Northern summer.

expect. Spring and fall show more equatorially symmetric flows, with a Hadley cell that has rising motion near the equator and subsidence in both hemispheres. However, the symmetric Hadley circulation is significantly weaker than the cross-equatorial circulation.

The equatorially asymmetric Hadley circulation bears some relationship to the monsoon flow. In particular, as we showed in an earlier problem, the effect of friction on the angular momentum of the cross-equatorial flow results in near-surface westerlies just to the south of the northern hemisphere convection. This effect is seen in figure14.6. Easterlies occur as a result of the quasi-conservation of angular momentum in the high-level return flow back across the equator. In the Asian monsoon the heating is displaced far to the north over the Asian continent, so the latitudinal extent and strength of the low-level southwesterly flow is much greater.

As we noted above, the meridional transport of heat by the atmosphere is a fundamental aspect of the atmospheric circulation. Figure 14.15 shows the mean meridional flux of moist entropy, multiplied by a reference temperature, which makes the units compatible with a moist enthalpy flux. The GFS model uses the dry entropy (log of potential temperature) as its fundamental thermodynamic variable, which means that entropy rather than energy is conserved by the model. Thus, we use entropy (disguised as energy) rather than energy. The moist entropy rather than the dry entropy flux is shown here because a significant fraction of the meridional heat transport is in the form of latent heat, i.e., water vapor which is added to the atmosphere at low latitudes and condensed out at high latitudes.

Figure 14.15 shows both the zonally symmetric transport and the eddy transport of entropy. The later dominates at all latitudes except between the equator and 10° N, where

the zonally symmetric part transports the bulk of the entropy. The flux toward the poles is strongest in the winter hemisphere, as one might expect, with peak transports near 40° S and 30° N. Thus, the region from 40° S to 30° N experiences a net gain of entropy from the sun and the surface, while higher latitudes experience net losses. The atmospheric transports exceed the estimates shown in figure 14.5, but are for a small segment of the opposite season.

The Ferrel cell is somewhat harder to understand than the Hadley circulation. The key is the flux form of the vorticity equation with friction. In spherical and pressure coordinates the vorticity equation is

$$a\cos\phi\frac{\partial\zeta_a}{\partial t}+\frac{\partial}{\partial\lambda}\left[u\zeta_a+\frac{\partial v}{\partial p}\omega-F_y\right]+\frac{\partial}{\partial\phi}\left[\left(v\zeta_a-\frac{\partial u}{\partial p}\omega+F_x\right)\cos\phi\right]=0 \tag{14.6}$$

where a is the radius of the earth, λ is the longitude, ϕ is the latitude, (F_x, F_y) is the frictional force per unit mass, and the rest of the variables have their conventional meaning. Defining an overbar as the zonal and time average with a prime indicating a deviation from this average, we note that the x and t derivative terms disappear, resulting in

$$\frac{\partial}{\partial\phi}\left[\left(\overline{v\zeta_a}-\overline{\frac{\partial u}{\partial p}\omega}+\overline{F_x}\right)\cos\phi\right]=0. \tag{14.7}$$

Integrating results in the quantity in square brackets being constant. However, this constant must be zero because otherwise there would be a non-zero meridional flux of vorticity at the poles, resulting in a delta function vorticity source there. This for time and zonal means, we find that

$$\overline{v\zeta_a}-\overline{\frac{\partial u}{\partial p}\omega}+\overline{F_x}=0. \tag{14.8}$$

Splitting fields into zonal mean and eddy parts, $v=\overline{v}+v'$ etc., and realizing that $\overline{v'}$ etc. equals zero, we get

$$\left\{\overline{v}\,\overline{\zeta_g}-\frac{\partial\overline{u}}{\partial p}\overline{\omega}\right\}+\left\{\overline{v'\zeta_a'}-\overline{\frac{\partial u'}{\partial p}\omega'}\right\}+\overline{F_x}=\overline{F_s}+\overline{F_e}+\overline{F_x}=0. \tag{14.9}$$

The first term in curly brackets $\overline{F_s}$ we refer to as the *zonally symmetric inviscid transport* of vorticity, while the second term $\overline{F_e}$ is called the *eddy inviscid transport* of vorticity. The sum of these two terms we refer to as the *net inviscid transport*. The force term $\overline{F_x}$ we call the *viscous transport* of vorticity. The component containing ω in $\overline{F_s}$ is often small compared to the v term, so to zeroth order we can ignore it. To the extent that $\overline{\zeta_z}\approx f$, the symmetric inviscid transport is therefore just $\overline{F_s}\approx\overline{v}f$.

Figure 14.16 shows that the most intense inviscid transport of vorticity is limited primarily to the near-surface region and the tropopause. Aside from strong surface transport associated with the Hadley circulation in the tropics, significant inviscid transport occurs in the latitude range $40°-60°$, with the strongest transport confined to the winter (southern) hemisphere. As equation (14.8) indicates, this inviscid transport is exactly counterbalanced by transport associated with surface friction. The latitude range where this effect is strongest (outside of the Hadley circulation) is underneath the polar jet streams where the shear is strong and baroclinic instability is active.

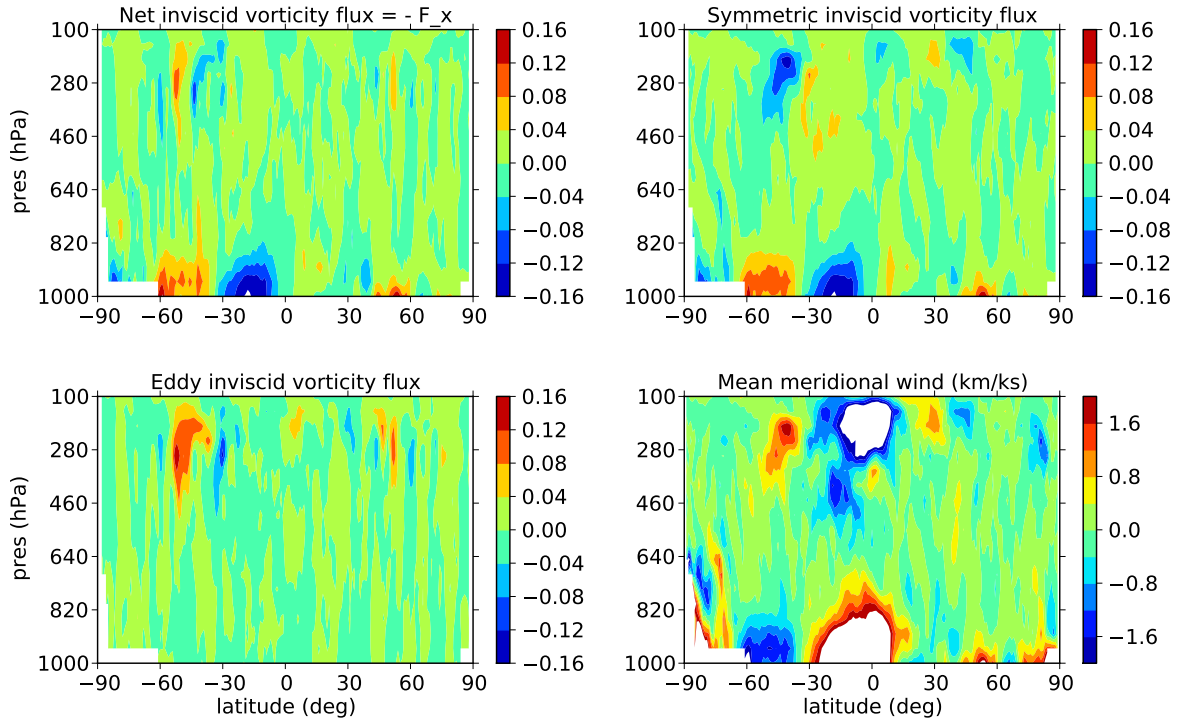

Figure 14.16: Plots related to the inviscid meridional transport of vorticity. The top left plot is the net meridional transport, top right is the transport due to the zonally symmetric circulation, bottom left is the meridional eddy transport of vorticity, bottom right is the zonal mean meridional wind scaled to show winds outside of the tropics.

From the top left panel of figure 14.16 one can infer that the friction at low levels under the jets is negative, or toward the west. This suggests that westerly (to the east) winds exist at the surface, a result which is confirmed by figure 14.6.

The top right and bottom left panels of figure 14.16 show that the low-level transport of vorticity is confined to the symmetric circulation, with little or no contributions from the eddies. The sign of the transport implies poleward meridional velocities in the middle latitudes of each hemisphere; this is confirmed in the bottom right panel of figure 14.16.

The net inviscid transport of vorticity at high levels is nearly zero, as the top left panel of figure 14.16 indicates. However, this hides the fact that the symmetric and eddy parts produce nearly equal and opposite meridional vorticity transports within the jet streams, with the eddy part moving positive vorticity toward the north pole and negative vorticity toward the south pole. The transport by the symmetric circulation at tropopause level implies flow toward the equator in both hemispheres in the region of jet streams. This is verified by the bottom right panel of figure 14.16.

The complete zonally symmetric circulation implied by the upper and lower regions of meridional flow under the jet streams is simply the Ferrel cell shown in figure 14.10. The

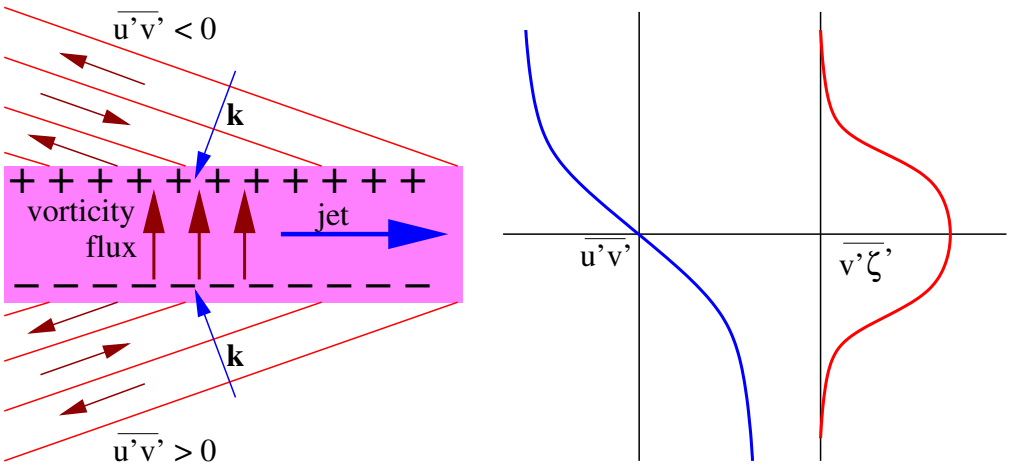

Figure 14.17: Schematic of processes responsible for the polar jet. The slanted lines north and south of the jet represent Rossby waves emitted by baroclinic instability in the jet region. The arrows between the wave fronts represent air motion due to the waves. These motions cause a convergence of the meridional momentum flux $\overline{u'v'}$ in the jet. This momentum flux convergence is associated with northward transport of vorticity, resulting depletion of vorticity on the south side of the jet and enhancement on the north side. This increases the meridional shear on the north and south sides of the jet, resulting in the acceleration of the jet.

above diagnostics show that all the pieces of the Ferrel cell and associated phenomena fit together. However, from the point of view of causality, they don't really tell us why the Ferrel cell is there. We now address this issue, using arguments taken from Vallis (2006).

Baroclinic instability is ubiquitous in the middle latitudes. It results from the interaction of the meridional surface temperature gradient and the tropospheric/stratospheric gradient of potential vorticity. This instability produces significant stirring of the atmosphere in the mid-latitude troposphere. This stirring results in the meridional emission of Rossby waves which propagate to the north and south away from the region of strong baroclinic instability. From the chapter on baroclinic instability, we find that Boussinesq Rossby waves of the form $\exp\left[i\left(kx + ly + m\xi - \omega t\right)\right]$ on a beta-plane with constant mean wind U have the dispersion relation

$$\omega = kU - \frac{\beta k}{k^2 + l^2 + m^2}. \tag{14.10}$$

The group velocity of Rossby waves in the meridional direction is

$$\frac{\partial \omega}{\partial l} = \frac{2\beta k l}{(k^2 + l^2 + m^2)^2}, \tag{14.11}$$

which means that northward-moving wave packets have $kl > 0$ while southward-moving packets have $kl < 0$. As we expect the group velocity of radiated Rossby waves to be away from the region of intense baroclinic instability,

Figure 14.17 shows how the orientation of the wave fronts results from the above conditions on kl. As Rossby waves are transverse waves, the air motions associated with the waves are parallel to the wave fronts, which results in $\overline{u'v'} > 0$ south of the jet and $\overline{u'v'} < 0$

on the north side. Thus, meridional convergence of zonal momentum occurs within the jet as a result of the momentum transport due to the radiated Rossby waves. This momentum convergence results in an effective force acting to accelerate the jet toward the east. This force is in the opposite sense of the surface frictional force, and by an argument similar to that used in the boundary layer, it results in a zonally symmetric equatorward flow through the jet. This equatorward symmetric flow is seen in the lower right panel of figure 14.16.

An alternate way of viewing the northward flux of vorticity through the jet core is via the relationship between $\overline{u'v'}$ and $\overline{v'\zeta'_a}$. By methods we have used before, it is easy to show that

$$\overline{v'\zeta'_a} \approx -\frac{\partial \overline{u'v'}}{\partial y} \tag{14.12}$$

The convergence in the momentum flux produces the meridional distribution of vorticity flux seen in figure 14.17. This vorticity flux enhances positive vorticity on the north side of the jet and depletes it on the south side, thus resulting in acceleration of the jet by the action of the baroclinic eddies. In a steady state the jet cannot accelerate, and the poleward flux of vorticity caused by the symmetric equatorward flow through the jet region compensates for the eddy-induced flux.

The eddy-induced convergence of momentum is responsible for the maintenance of the polar jet in this view. The vertical shear profile in the jet is determined by the thermal wind equation. Thus, if the polar jet at high levels is sufficiently strong, the surface winds are also westerly, which leads to the surface friction responsible for the poleward flow at low levels beneath the jet. Thus, the polar jet and the associated Ferrel cell can be seen to be a response to the concentrated baroclinic instability occurring at mid-latitudes.

14.5 References

Peixoto, J. P., and A. H. Oort, 1992: *Physics of Climate.* American Institute of Physics, New York, 520 pp. This contains a lot of good climatological information.

Reynolds, R. W., and D. C. Marsico, 1993: An improved real-time global sea surface temperature analysis. *J. Climate*, **6**, 114-119.

Vallis, G. K., 2006: *Atmospheric and oceanic fluid dynamics.* Cambridge University Press, 745 pp. Vallis discusses the Hadley and Ferrel cells in chapter 11 and the mean zonal circulation in chapter 12.